

Kagomerization of transition metal monolayers induced by two-dimensional hexagonal boron nitride

Hangyu Zhou^{1,2,3,4,†}, Manuel dos Santos Dias^{1,5,6}, Youguang Zhang², Weisheng Zhao^{3,‡}, and Samir Lounis^{1,5,*}

¹Peter Grünberg Institut and Institute for Advanced Simulations, Forschungszentrum Jülich & JARA, 52425 Jülich, Germany

²School of Electronic and Information Engineering, Beihang University, Beijing 100191, China

³Fert Beijing Institute, School of Integrated Circuit Science and Engineering, Beihang University, Beijing 100191, China.

⁴Shenyuan Honors College, Beihang University, Beijing 100191, China

⁵Faculty of Physics, University of Duisburg-Essen and CENIDE, 47053 Duisburg, Germany

⁶Scientific Computing Department, STFC Daresbury Laboratory, Warrington WA4 4AD, United Kingdom

[†]hangyu.zhou@buaa.edu.cn

[‡]weisheng.zhao@buaa.edu.cn

*s.lounis@fz-juelich.de

The kagome lattice is an exciting solid state physics platform for the emergence of nontrivial quantum states driven by electronic correlations: topological effects, unconventional superconductivity, charge and spin density waves, and unusual magnetic states such as quantum spin liquids. While kagome lattices have been realized in complex multi-atomic bulk compounds, here we demonstrate from first-principles a process that we dub kagomerization,

in which we fabricate a two-dimensional kagome lattice in monolayers of transition metals utilizing a hexagonal boron nitride (*h*-BN) overlayer. Surprisingly, *h*-BN induces a large rearrangement of the transition metal atoms supported on a fcc(111) heavy-metal surface. This reconstruction is found to be rather generic for this type of heterostructures and has a profound impact on the underlying magnetic properties, ultimately stabilizing various topological magnetic solitons such as skyrmions and bimerons. Our findings call for a reconsideration of *h*-BN as merely a passive capping layer, showing its potential for not only reconstructing the atomic structure of the underlying material, e.g. through the kagomerization of magnetic films, but also enabling electronic and magnetic phases that are highly sought for the next generation of device technologies.

Introduction

The kagome lattice is a two-dimensional (2D) network of corner-sharing triangles which offers a fertile ground for exploring geometry, correlations, and topology in condensed matter physics ¹. The frustration arising from the constituent triangular units leads to the emergence of frustrated magnetic order ²⁻⁴ and spin liquid phases ^{5,6}, as well as exotic electronic structures ^{7,8}. The frustrated geometry leads to the emergence of flat bands associated with electron localisation, which are expected to increase the correlation effects and support many-body electronic phases and novel topological phases including ferromagnetism ⁹⁻¹¹, unconventional superconductivity ^{12,13}, and fractional quantum Hall states ^{14,15}, to name only a few. Magnetic kagome lattices, especially in the 3d transition metal compounds, display intrinsic anomalous Hall effects driven by various mecha-

nisms^{16–19}.

In recent years, 3*d* transition metal kagome structures have been reported for several materials²⁰, including CoSn^{21,22}, FeSn^{8,23}, Fe₃Sn₂^{3,24,25}, Mn₃Sn^{19,26}, Co₃Sn₂S₂^{4,27,28}, and AV₃Sb₅ (*A* = K, Rb, and Cs)^{13,29–32}. While these systems are interpreted as demonstrations of the physics of 2D kagome lattices, their bulk nature makes the connection less transparent³³. Moreover, monolayer vanadium-based kagome metals are predicted to be thermodynamically stable and to have distinct properties compared to their three-dimensional bulk forms³⁴, demonstrating the importance of dimensionality for kagome materials. Therefore, materials that indeed comprise just a single kagome layer can serve as an ideal platform for prototypical realization of the electronic structures and novel phenomena arising from reduced dimensionality. However, to achieve this goal we must overcome the scarcity of genuinely 2D kagome materials.

Even though we are interested in achieving a truly 2D kagome material, in reality it will have to be deposited on a surface and likely covered with some other protective material. In this context, two popular and quite distinct encapsulation materials are graphene and *h*-BN. While graphene is a semimetal, *h*-BN is a large band gap insulator which makes it a suitable substrate and encapsulation layer rather than a functional material for spintronic applications^{35–39}. However, recent studies have shown that *h*-BN can have a substantial impact on the encapsulated material, leading for instance to sizeable Rashba effect and Dzyaloshinskii-Moriya interaction (DMI) when interfaced with magnetic materials^{40–42}.

In this work, we show that it is feasible to realize a monolayer kagome lattice with the as-

sistance of *h*-BN, a novel structural rearrangement which we term kagomerization. Using density functional theory (DFT), we demonstrate that *h*-BN can serve a functional role in facilitating remarkable structural reconstructions of transition metals. In particular, we find that kagomerization is rather universal when the epitaxial 3*d* transition metal monolayer (abbreviated as the TM layer) is grown on heavy metal (HM) fcc (111) surfaces, as unveiled for Pt, Au, and Ag substrates, as illustrated in Fig. 1a. We rationalize this general behaviour by analyzing the contributions from *h*-BN, substrates and the TM-TM bond lengths. Subsequently, we focus on the structures containing ferromagnetic (FM) elements Fe, Co, or Ni. We identify electronic hallmarks expected for the kagome lattice such as Dirac cones and flat bands. Moreover, we investigate the effect of this kagomerization on the magnetic properties and magnetic interactions. The frustrated Heisenberg exchange interactions, competing with DMI and magnetocrystalline anisotropy, lead to the formation of topological spin textures, such as skyrmions and bimerons, which are promising for the next generation of data storage devices⁴³⁻⁴⁵. The spin textures discovered in kagome monolayers, in particular the bimerons, manifest a plethora of magnetic phases responsive to applied magnetic fields. These discoveries offer new opportunities for further experimental exploration aimed at realizing an individual kagome lattice and stabilizing complex spin-textures.

Results

Kagomerization induced by *h*-BN. The considered structure consists of a 3*d* TM monolayer grown on fcc(111) HM (Pt, Au, Ag) substrates with a capping *h*-BN layer, as depicted in Fig. 1a. The experimental lattice constant for *h*-BN is 2.504 Å⁴⁶, which is substantially smaller than the

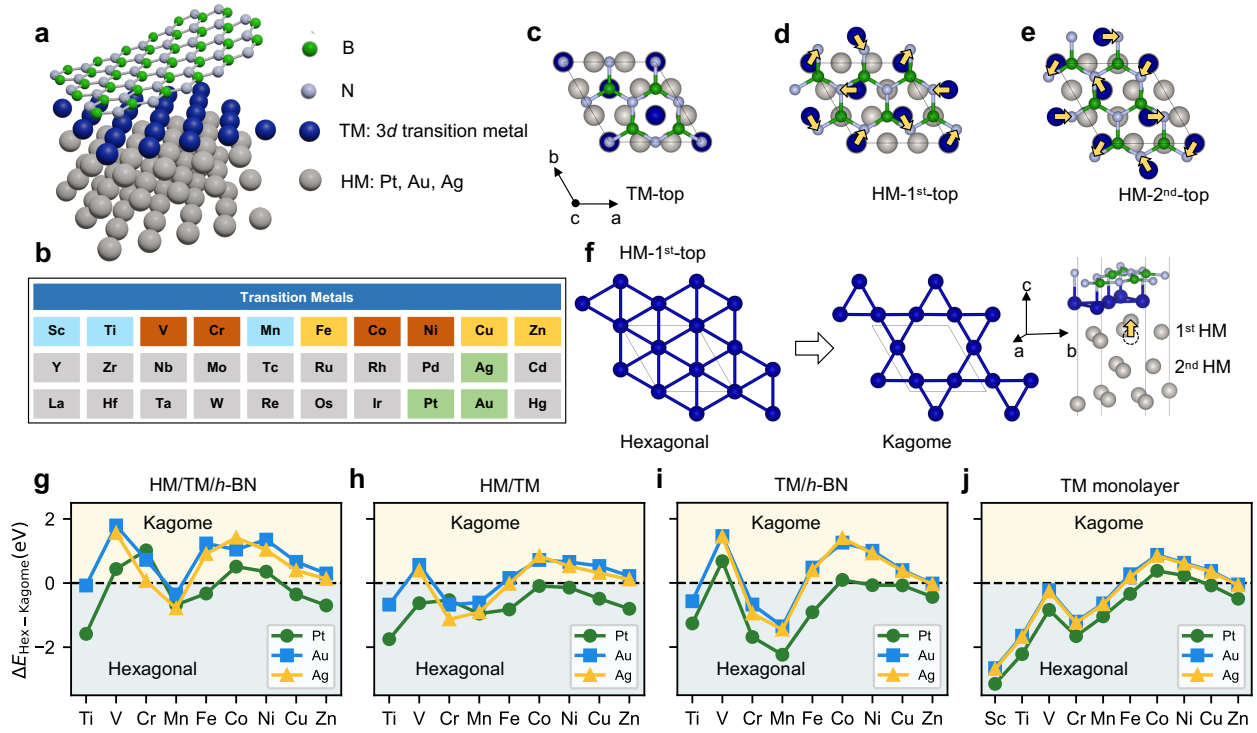


Figure 1: Kagomerization of transition metal monolayers on heavy-metal substrates.

a Schematic representation of the fcc(111) heavy-metal (HM) substrate with an epitaxial 3d transition metal (TM) monolayer, capped by *h*-BN. **b** Considered portion of the periodic table. Elements shaded in grey were not investigated. **c-e** Three stacking configurations that have both a N and a B atom directly on top of: **c** the TM atoms (TM-top); **d** the interfacial HM atoms (HM-1st-top); or **e** the sub-interfacial HM atoms (HM-2nd-top). **f** Reshaping of the TM layer in the HM-1st-top structure from a hexagonal to a kagome lattice, shown in top and side views. **g-j** Energy differences between the hexagonal and the kagome structures of the TM monolayer: **g** for the complete heterostructure; **h** without *h*-BN; **i** without the HM; **j** without *h*-BN and the HM. Positive (negative) values indicate an energetic preference for the kagome (hexagonal) structures. For Sc on all surfaces and for Ti on Ag the initial kagome structure reverted back to the hexagonal one, so no data is shown.

experimental lattice constant of the surface fcc(111) unit cell of Pt (2.775 Å⁴⁷), Au (2.884 Å⁴⁸) and Ag (2.889 Å⁴⁹). Taking the lattice mismatch and the significantly weaker interaction of *h*-BN with the metal surface in comparison to the strong σ -bonds between N and B atoms⁵⁰ into account, a low-strain scenario consists of a 2×2 supercell of *h*-BN grown on a $\sqrt{3} \times \sqrt{3} R30^\circ$ TM/HM (Pt, Au, Ag), which are commonly found at *h*-BN/HM(111) interfaces^{51,52}. From our DFT calculations the lattice mismatch in this scenario is about 3.2% for Pt, 1.3% for Au, and 0.9% for Ag, respectively. We systematically studied all *3d* transition metal monolayers with three different HM substrates (Pt, Au, Ag), as highlighted in Fig. 1b. We discover that the kagomerization is a rather universal behavior among the explored materials. It can occur spontaneously even when starting from a non-kagome stacking configuration and can often be the ground state.

In Fig. 1c-e, we illustrate three different starting configurations for our heterostructures. By performing a DFT relaxation of these structures, we find that the TM atoms always move underneath N atoms, as indicated by the yellow arrows in Fig. 1d,e, except for the TM-top structure, Fig. 1c. This behavior parallels previous findings on Ni(111) and Co(0001) surfaces capped by *h*-BN, for which the favorable binding configuration is also found to be N (B) atoms standing directly on top of the transition metal atom (hollow sites), respectively^{53,54}. Due to the electrostatic landscape created by the *h*-BN monolayer, a kagome lattice is obtained from the HM-1st-top structure (see Fig. 1f), while the HM-2nd-top structure leads to a distorted hexagonal lattice (see Supplementary Fig. S1), and the TM-top structure maintains the ideal hexagonal lattice. In the obtained kagome lattice all N atoms of the unit cell are on top of a TM atom, except for one N that instead attracts one HM atom from the substrate towards the hexagonal hole of the kagome lattice.

Fig. 1g shows the total energy difference between the relaxed hexagonal and kagome structures, where positive (negative) values indicate a kagome (hexagonal) ground state, respectively. We find that V, Cr, Co and Ni monolayers (highlighted in red in Fig. 1b) form a kagome lattice as the ground state on top of the three investigated substrates, while for the Fe, Cu and Zn monolayers this happens only on the Ag and Au surfaces (yellow boxes in Fig. 1b). In some cases (e.g. V and Cr on Pt), although the kagome structure is the ground state, none of the starting configurations shown in Fig. 1c-e relaxes to it, which likely indicates the existence of an energy barrier. Lastly, Sc and Ti are found to never favour the kagome structure. More details about the spontaneity and ground state can be found in Supplementary Fig. S2, while Supplementary Fig. S3 provides more information about various structural parameters.

To identify the mechanisms leading to the kagomerization, we analyse the energy differences plotted in Fig. 1g. First, one immediately recognizes that the likeliness to fabricate a kagome lattice is enhanced when Au and Ag substrates are utilized. Second, the energy differences across the family of transition elements show an M-shape, with a two-peak feature close to the edges of the transition metal series and a minimum around half-filling, i.e., in the middle of the series. This behavior is a signature of a *d*-band-filling effect, which is also used to rationalize the trends of their cohesion^{55,56} and surface energies^{57,58}. These findings suggest that the tendency of a given transition metal towards forming a kagome structure can be estimated from its placement in the periodic table.

To gain some insights into the role played by *h*-BN, we split the heterostructures by removing

either *h*-BN or the metal surface, but keeping all remaining atoms in their prior optimized positions. In Fig. 1h, we plot the total energy differences between the hexagonal and kagome structures when *h*-BN is removed. While for Pt the hexagonal structure is always lower in energy, for Ag and Au the kagome structure still has a lower energy for several elements. This is likely due to a combination of the weaker binding between the TM atoms and Ag or Au and the large effective strain from the mismatch between the surface lattice parameter and the equilibrium TM-TM bond lengths. In Fig. 1i, we plot the total energy differences between the hexagonal and kagome structures when instead the HM surface is removed. The trend for whether the kagome or the hexagonal structures have lower energy is broadly similar to what was previously found in the calculations for the complete heterostructures, which points to *h*-BN being indeed the main driver for the kagomerization. As a final check, we consider the energetics of the free-standing monolayer, shown in Fig. 1j. When the monolayers are strained to match the lattice constants of the absent surfaces the hexagonal structure is favored for most elements, however the kagome structure is preferred for the transition metals going from Fe to Cu. This shows that there is an intrinsic component to the kagomerization, which can be enhanced by the combination of surface-driven strain and hybridization with *h*-BN.

To summarize, we found that the kagomerization is a fairly generic behaviour for the studied heterostructures. Due to the electrostatic landscape created by *h*-BN, TM atoms interact with *h*-BN and experience an effective attraction towards their closest N atom. However, the TM atoms are also bound to the surface, which can hinder the expected motion towards N. As the interaction of the TM atoms with the surface is weaker for the Ag and Au cases than for the Pt case, so is

the kagomerization more energetically favored for the noble metal surfaces. Another factor that contributes to the stabilization of the kagome structure is its shorter nearest-neighbor distance in comparison to the ideal hexagonal structure. This can alleviate some of the strain that the TM atoms are subject to when forced to adopt the lattice parameter of the HM surfaces. Our results provide a practical method to realize the 3*d* transition metal kagome monolayer and establish a platform for studying intriguing 2D physics.

Flat bands and Dirac cones. Having established that TM monolayers can adopt a stable kagome lattice, we first turn to its expected electronic fingerprints, which are Dirac cones and flat bands according to simple nearest-neighbour tight-binding models. We choose FM Co as a representative case, and compare the spin-resolved band structure of the ideal monolayer kagome lattice (Fig. 2a) with the projected band structure of Pt/Co/*h*-BN (Fig. 2b) and Ag/Co/*h*-BN (Fig. 2c). For the ideal kagome lattice, we can identify rather flat bands at about 0.5 eV and -0.8 eV in Fig. 2a and also Dirac-like bands such as a Dirac cone slightly below the Fermi energy at the K point. The band structure of Pt/Co/*h*-BN (see Fig. 2b) is more complex, mostly due to additional *d*-like bands coming from the HM, but we can discern a flat minority Co band (dark blue line) at about 0.15 eV below the Fermi level at the Γ point and a Dirac crossing at about 0.3 eV above the K point, just to give two examples. For Ag/Co/*h*-BN the picture is clearer as Ag only contributes a few *s*-like bands and its hybridisation with the TM is weaker than Pt, and multiple flat bands and Dirac cones are visible in Fig. 2c. Other band structure examples are collected in Supplementary Fig. S4. We conclude that the fundamental electronic aspects expected for a kagome lattice are indeed found in the discussed kagomerized monolayers, which hence offer a new platform for the investigation of

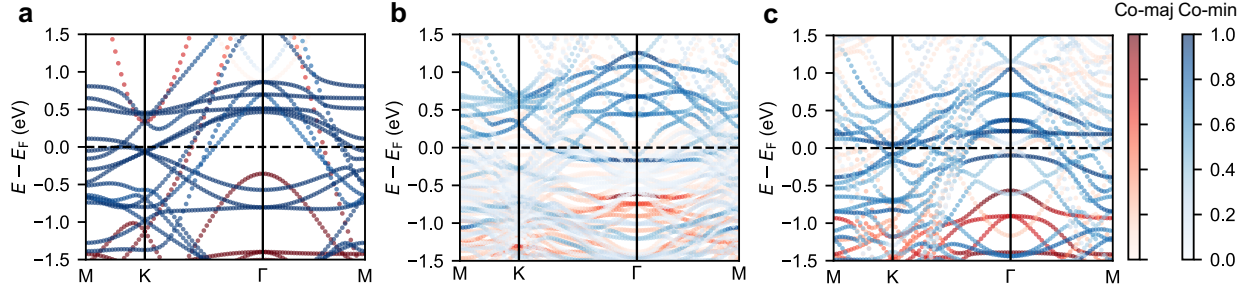


Figure 2: Spin-resolved projected band structures of kagomerized Co layers. Spin- and Co-projected band structures for: **a** isolated Co monolayer kagome lattice; **b** Pt/Co/*h*-BN; and **c** Ag/Co/*h*-BN. The color bar encodes the weight of Co majority states and minority spin states.

potential correlated topological phases.

Impact of kagomerization on magnetic properties and magnetic interactions. We now discuss the kagome-related changes to the TM magnetism, concentrating on FM Fe, Co and Ni for simplicity. We first compare the spin moments for the HM/TM (hexagonal, labelled w/o-BN-Hex) and for the HM/TM/*h*-BN (kagome, labelled w/-BN-Kagome) structures. The overall trend is for a reduction when going from the hexagonal to the kagome structure (for instance, the spin moment of Fe on Au reduces from $3.09 \mu_B$ to $2.78 \mu_B$), and we gather all the values in Supplementary Table S1. The question arises as to whether this reduction is driven mostly by the structural rearrangement (and the attending shortening of the TM nearest-neighbor distances), by the hybridization with *h*-BN, or by a combination of both. As this will also be pertinent for the magnetic interactions, we devise two auxiliary structures to acquire additional data. The w/-BN-Hex structure is obtained from the HM/TM structure by introducing the *h*-BN overlayer while maintaining the HM layer in the hexagonal arrangement, and the w/o-BN-Kagome structure by removing the *h*-BN overlayer

from the full kagome structure. These four structures are illustrated in Supplementary Fig. S5. We computed the pairwise magnetic interactions, including Heisenberg exchange (J) and DMI (D), for all structures (see Methods section).

We select the Pt/Co system to illustrate the changes to the magnetic interactions due to the kagomerization before presenting a systematic overview. Fig. 3a shows the spatial distribution of J for the epitaxial Co on Pt structure (w/o-BN-Hex) with C_{3v} symmetry. Each circle represents a Co atom and is colored as a function of the J values with respect to the central Co (grey circle), which is taken as reference. The value of J is given by the color scale, with red (blue) for ferromagnetic (antiferromagnetic) coupling. Fig. 3b depicts the results obtained for the w/o-BN-Kagome structure. The nature of the interactions as a function of the distance is similar to the hexagonal case. The results for the structures that include the h -BN overlayer are shown in Fig. 3c-d, but to make a comparison we also compute the differences to the results obtained without the overlayer, for the same arrangement of Co atoms. This is presented in Fig. 3e-f, with the purple (green) color revealing an increase (decrease) of J after capping with h -BN. The largest absolute change in the interactions takes place for the nearest-neighbor pairs, as these are the strongest interactions. For example, the nearest-neighbor interactions in the w/-BN-Kagome structure are 4 meV larger than in the w/o-BN-Kagome structure, a relative change of 14%. However, the largest relative changes occur for larger distances for which the interactions are small in magnitude.

An alternative way of quantifying the differences in the magnetic interactions between the different structures is by computing the respective micromagnetic parameters, defined in the Meth-

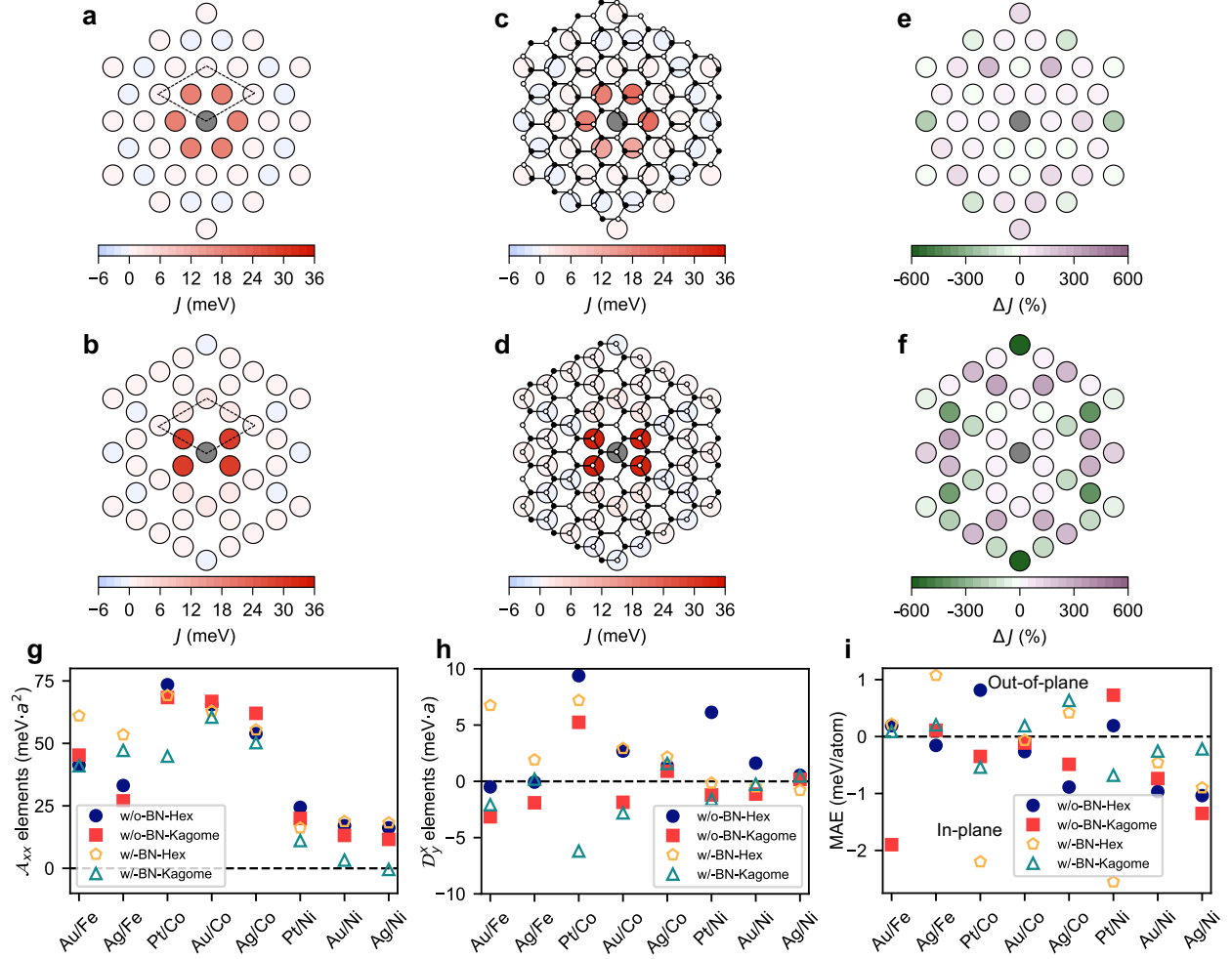


Figure 3: Impact of kagomerization on the magnetic interactions and magnetic anisotropy

energy (MAE). **a-d** Spatial distribution of the Heisenberg exchange interactions for the four considered structures in the Pt/Co system. The unit cell is shown by dashed black lines and contains three Co atoms in all cases. The Co atom shaded in grey is taken as the reference atom and the color of the surrounding circles indicates the value of J for the corresponding pair. The positive (negative) values correspond to ferromagnetic (antiferromagnetic) coupling. Shown are the **a** w/o-BN-Hex, **b** w/o-BN-Kagome, **c** w/-BN-Hex, and **d** w/-BN-Kagome structures. The small white and black circles represent N and B atoms, respectively. **e-f** Relative differences in J values of Pt/Co system for the structures with and without h -BN. **e** corresponds to **c** minus **a**. **f** corresponds to **d** minus **b**. Micromagnetic parameters: **g** Exchange stiffness tensor elements A_{xx} ; **h** DMI spiralization tensor elements D_y^x . a is the lattice parameter of the surface unit cell. **i** MAE per magnetic atom. Positive (negative) values correspond to out-of-plane (in-plane) anisotropy.

ization tensor elements D_y^x . a is the lattice parameter of the surface unit cell. **i** MAE per magnetic atom. Positive (negative) values correspond to out-of-plane (in-plane) anisotropy.

ods. As the sums run over all the magnetic atoms, the micromagnetic quantities have the symmetry of the point group, which is higher than the symmetry of the pairwise interactions shown in Fig. 3b-d, and results in only two independent parameters (one for the stiffness and one for the spiralization). The long-range part of the pairwise interactions makes a very important contribution to the micromagnetic parameters (see Supplementary Note 5 and Supplementary Fig. S6a), so it cannot be neglected. Fig. 3g shows the independent parameter \mathcal{A}_{xx} for the stiffness tensor for the considered systems (by symmetry, $\mathcal{A}_{yy} = \mathcal{A}_{xx}$ and all others are zero). Looking first at the results for the Pt/Co system and taking the value obtained for the w/o-BN-Hex structure as reference, we find a modest change in \mathcal{A}_{xx} except for the realistic w/-BN-Kagome structure for which there is a 39% reduction. This is explained by the changes in the long-range part of the Heisenberg exchange that were mapped in Fig. 3f. This strong reduction cannot be explained either by the formation of the kagome structure or by the hybridization with *h*-BN, and is clearly a combined effect of the two. The nature of the surface also plays an important role, as this strong change in \mathcal{A}_{xx} is not seen for the Au/Co and Ag/Co systems. This synergy between structural rearrangement and hybridization is even more prominent for the Ni systems, for which we found an almost complete suppression of \mathcal{A}_{xx} for Au/Ni and Ag/Ni due to a strong enhancement in antiferromagnetic character of the long-range interactions. Lastly, the case of Ag/Fe shows that a significant strengthening of \mathcal{A}_{xx} due to hybridisation with *h*-BN is also possible.

The properties of the pairwise DMI are nicely condensed in their micromagnetic counterpart, the DMI spiralization tensor (see Methods), which thanks to the point group symmetry only has one independent parameter \mathcal{D}_y^x ($\mathcal{D}_x^y = -\mathcal{D}_y^x$ and all other elements are zero). Fig. 3g shows the val-

ues of \mathcal{D}_y^x for all considered structures. Pt has a strong spin-orbit coupling and hybridises strongly with the magnetic atoms, which leads to the strong DMI found for Co and Ni in the w/o-BN-Hex structure, while the weaker hybridization for Au and the weaker spin-orbit coupling of Ag explain the weaker DMI values found in those systems. In contrast, spin-orbit coupling is negligible for *h*-BN, so its strong impact on the DMI values is driven both by the structural rearrangement of the magnetic atoms and by modifications to their hybridisation with the surface. We first demonstrate that the DMI is quite susceptible to the structural rearrangement from hexagonal to kagome. Comparing \mathcal{D}_y^x in the w/o-BN-Hex and w/o-BN-Kagome structures, we even find that the DMI chirality is reversed in the Au/Co, Pt/Ni and Au/Ni systems. The modifications to the DMI are even stronger for the Pt/Co system, but only once *h*-BN is accounted for. The hybridization with *h*-BN can even induce sizeable DMI for systems where it was originally negligible, such as Au/Fe and Ag/Fe.

The final aspect to consider is the modification of the magnetic anisotropy energy (MAE) by *h*-BN. The MAE for all the structures is shown in Fig. 3i. Positive values indicate an out-of-plane and negative values an in-plane anisotropy, respectively. Going from the w/o-BN-Hex structure to the w/-BN-Kagome one can even lead to a change in the nature of the MAE, from out-of-plane to in-plane for Pt/Co and Pt/Ni and in reverse for Ag/Fe, Au/Co, Ag/Co (and almost for Ag/Ni). Overall, we conclude that the kagomerization of the TM layer driven or stabilized by *h*-BN leads to quantitative and often qualitative changes in the various considered magnetic interactions, and so we also expect strong changes to the magnetic states found for each system.

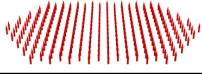

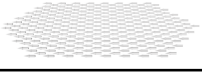
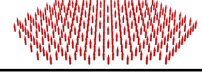
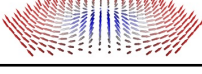
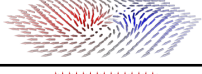

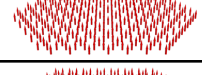
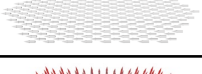
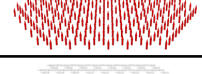
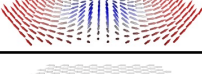
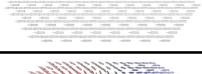
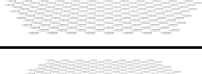
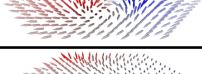


Hexagonal lattice			Kagome lattice		
Au/Fe	Ferromagnetic		Au/Fe/ <i>h</i> -BN	Skyrmions	
Ag/Fe	Ferromagnetic		Ag/Fe/ <i>h</i> -BN	Ferromagnetic	
Pt/Co	Skyrmions		Pt/Co/ <i>h</i> -BN	Bimerons	
Au/Co	Ferromagnetic		Au/Co/ <i>h</i> -BN	Ferromagnetic	
Ag/Co	Ferromagnetic		Ag/Co/ <i>h</i> -BN	Ferromagnetic	
Pt/Ni	Skyrmions		Pt/Ni/ <i>h</i> -BN	Ferromagnetic	
Au/Ni	Ferromagnetic		Au/Ni/ <i>h</i> -BN	Bimerons	
Ag/Ni	Ferromagnetic		Ag/Ni/ <i>h</i> -BN	Bimerons & spirals	

Figure 4: Magnetic states for various heterostructures. Magnetic states found for the magnetic monolayers on heavy-metal surfaces and their modification by *h*-BN. These were obtained from atomistic spin dynamic simulations employing the magnetic interactions for the two realistic structures, w/o-BN-Hex and w/-BN-Kagome.

Spin textures and their evolution in a magnetic field. Fig. 4 summarizes the magnetic states found by atomistic spin dynamics simulations utilizing the full set of magnetic interactions obtained for the two realistic structures, w/o-BN-Hex and w/-BN-Kagome. Without h -BN we find ferromagnetic states for most systems, which are in-plane or out-of-plane according to the respective MAE, with the exception of the Pt systems for which the DMI is strong enough to enable metastable skyrmionic states. h -BN changes the magnetic states for different systems in different ways. In the Pt/Co case, skyrmions turn into bimerons due to the change of sign of the MAE, while for the Pt/Ni case an in-plane ferromagnetic state is stabilized by a combination of reduced DMI and strengthened in-plane MAE. (We remark that a bimeron can also be referred to as an asymmetric skyrmion⁵⁹ or in-plane skyrmion^{60,61}.) We also found qualitative changes in the magnetic state for three other systems. Skyrmions appear for Au/Fe due to the enhanced DMI, while for Au/Ni and Ag/Ni bimerons appears due to a weakening of the MAE and a dramatic suppression of the exchange stiffness. In the Ag/Ni system this suppression is strong enough to destabilize the ferromagnetic state itself in favor of a spin spiral.

Next we investigate the response of the various spin textures to an applied magnetic field. The considered zero-field spin textures are presented in Fig. 5a-c. For Pt/Co/ h -BN (Fig. 5a) and Au/Co/ h -BN (Fig. 5b), bimerons prefer to be in the head-to-head configuration and connect with each other. To compare with the more familiar skyrmion picture, we uniformly rotate the magnetization by 90° so that its ferromagnetic component is along the z -axis, obtaining the distorted skyrmion state shown in the insets. This establishes that the bimerons themselves are asymmetric. The situation is more complex for Ag/Ni/ h -BN (Fig. 5c), where we find merons and antimerons

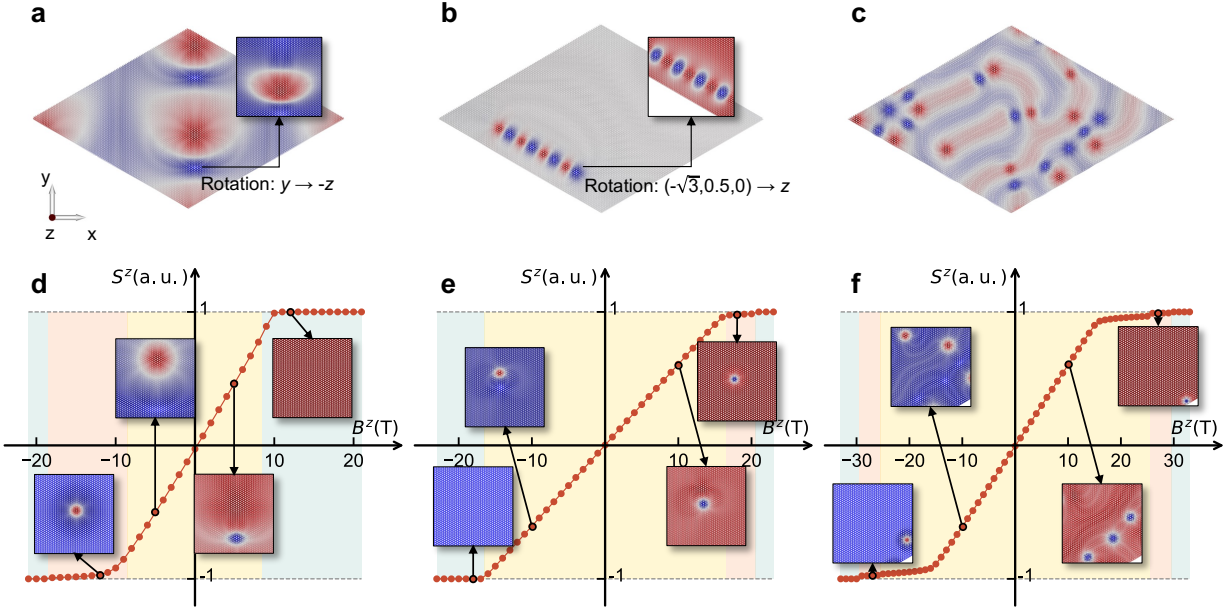


Figure 5: Manipulating spin textures with a magnetic field. **a-c** Spin textures in zero external magnetic field: **a** Bimerons in Pt/Co/h-BN; **b** Bimeron chain in Au/Ni/h-BN; **c** Spirals with trapped bimerons in Ag/Ni/h-BN. **d-f** Evolution of spin textures with a magnetic field, traced with the total z component of the magnetization: **d** Pt/Co/h-BN; **e** Au/Ni/h-BN; **f** Ag/Ni/h-BN. We identify three regions with different colors: yellow, pink, and blue blocks indicate the regions where bimeron, skyrmion, and uniform ferromagnetism occur, respectively. The insets show examples of the corresponding magnetic states. The spins are colored as follows: red is $+z$, blue is $-z$, and grey is in-plane.

trapped in spin spirals. The total number of merons or antimerons in the system is always even, so we refer to them as bimerons.

The obtained bimerons are stabilized by the combination of interface-induced DMI and in-plane anisotropy, which leads to their discussed asymmetry, and will also lead to different responses to external fields applied along the $+z$ or $-z$ directions. The evolution of the spin textures with the applied field is summarized in Fig. 5d-f. This evolution can be divided into three regions indicated by different colors. Bimerons exist in the yellow region, and for increasing magnitude of the applied field they deform and become progressively more similar to skyrmions or anti-skyrmions. Skyrmions exist in the pink region, which only appears for a given sign of the magnetic field but not for the opposite one in Fig. 5d-e. This is due to the asymmetry of the bimerons, which causes them to annihilate in the ferromagnetic state for the unfavorable sign of the magnetic field. The situation is qualitatively distinct for Ag/Ni/*h*-BN (Fig. 5c) as the bimerons exist in a spin spiral background. This introduces a compensation in the possible types of asymmetry for the bimerons, so that some can always evolve into skyrmions irrespective of the sign of the applied field. One could then characterize the yellow region in Fig. 5f as containing bimerons which are in a sense precursors of skyrmions or antiskyrmions which would arise in the applied field, the skyrmions surviving into the pink regions and the antiskyrmions annihilating into the ferromagnetic state.

Discussion

We identified through first-principles simulations a spontaneous rearrangement of transition metal atoms on a heavy-metal surface catalysed by an *h*-BN overlayer — a process that we named kagomerization. The selected heavy-metal surfaces (Pt, Au and Ag) were chosen due to the small lattice mismatch between a 2×2 supercell of *h*-BN and a $\sqrt{3} \times \sqrt{3} R30^\circ$ surface unit cell. We anticipate that kagomerization can also take place on other surfaces. In fact, there is a recent experimental report of a monolayer Ni kagome lattice forming on Pb(111), which was found to be non-magnetic⁶². We also note that two-dimensional magnetic kagome lattices can be obtained by mechanical exfoliation of van der Waals materials, for instance $\text{Pd}_3\text{P}_2\text{S}_8$ ⁶³ and Nb_3Cl_8 ⁶⁴. Here our focus is on more conventional heterostructures that are routinely grown for spintronics experiments, concentrating on material combinations which preserve their magnetism and have a higher likelihood of being experimentally realized. The band structure of the kagomerized structures shows the expected flat band and Dirac cone features, which should provide opportunities to study the interplay between geometry, topology, and magnetism.

The central aspect of our study is the systematic study of how the kagomerization modifies the magnetic properties of the transition metal monolayers. We selected three ferromagnetic elements, Fe, Co and Ni, and adopted a two-pronged approach based on extracting all the relevant magnetic interactions from first-principles calculations combined with an exploration of the magnetic states through atomistic spin dynamics. Our analysis shows that *h*-BN often has a strong quantitative and even qualitative effect on the magnetic interactions, challenging its as-

sumed role as a passive capping layer. Both the spin-orbit-driven magnetic anisotropy energy and Dzyaloshinskii-Moriya interactions as well as the typically much stronger Heisenberg exchange interactions can be strongly modified by the kagomerization. This enables switching between different magnetic states, such as from skyrmions to bimerons, or from ferromagnetic to spiralling states, by the addition of an *h*-BN overlayer. Furthermore, we unveiled the asymmetric response of the bimerons under external magnetic fields applied along the positive and negative *z* directions.

Our prediction of kagomerization of transition metal layers by *h*-BN and the surprisingly strong impact on their magnetic properties opens exciting perspectives for spintronics. Besides exploring the properties of the homogeneous heterostructures and their tunability with an applied magnetic field, additional prospects are opened by creating areas with and without the *h*-BN overlayer, for instance by lithography. These different areas can host very different magnetic states, and could act as spintronic circuit elements for skyrmion or bimeron injection or annihilation, among other possibilities. The combination of fundamental physics with prospects for innovative device concepts will make this type of heterostructure very appealing for future investigations.

Methods

First-principles calculations

Optimization of the considered structures was performed using the density functional theory (DFT) approach implemented in the Quantum Espresso computational package ⁶⁵, including the van der Waals correction (DFT-D3 ⁶⁶). We employed the projector augmented wave pseudopotentials from the pslibrary ⁶⁷, with the generalized gradient approximation of Perdew, Burke and Ernzerhof

(PBE) ⁶⁸ as the exchange and correlation functional. Convergence tests led to a plane-wave energy cut-off of 90 Ry and an $18 \times 18 \times 1$ k-point grid. We optimize the lattice constant of the HM substrates and use those values for the heterostructures with TM layers and with or without *h*-BN.

The magnetic properties and magnetic interactions were computed using the all-electron full-potential scalar-relativistic Korringa-Kohn-Rostoker (KKR) Green function method ^{69,70} including spin-orbit coupling self-consistently as implemented in the JuKKR computational package. The angular momentum expansion of the Green function was truncated at $\ell_{\max} = 3$ with a k-mesh of $18 \times 18 \times 1$ points. The energy integrations were performed including a Fermi-Dirac smearing of 502.78 K, and the local spin-density approximation was employed ⁷⁰. The Heisenberg exchange interactions and DM vectors were extracted using the infinitesimal rotation method ^{71,72} with a finer k-mesh of $80 \times 80 \times 1$ and real-space cutoff radii of $R = 14a$ for Fe and $R = 8a$ for Co and Ni (a is the lattice parameter of the surface unit cell).

Magnetic interactions and atomistic spin dynamics

We consider a classical extended Heisenberg Hamiltonian including Heisenberg exchange coupling (J), DMI (\mathbf{D}), the magnetic anisotropy energy (K), and Zeeman term (\mathbf{B}). All parameters were obtained from first-principles calculation. The spin-lattice model reads as follows:

$$E = - \sum_{i,j} J_{ij} \mathbf{S}_i \cdot \mathbf{S}_j - \sum_{i,j} \mathbf{D}_{ij} \cdot (\mathbf{S}_i \times \mathbf{S}_j) - \sum_i \mathbf{B} \cdot \mathbf{S}_i - \sum_i K_i (S_i^z)^2 . \quad (1)$$

where \mathbf{S}_i and \mathbf{S}_j are the magnetic moments of unit length at position \mathbf{R}_i and \mathbf{R}_j respectively.

We will transform the obtained pairwise magnetic interactions into the parameters of the

following micromagnetic energy functional:

$$E_{\text{micro}} = \frac{1}{V_0} \int d\mathbf{r} \left[\frac{1}{2} \sum_{\alpha, \beta} \mathcal{A}_{\alpha\beta} \frac{\partial \mathbf{m}(\mathbf{r})}{\partial r^\alpha} \cdot \frac{\partial \mathbf{m}(\mathbf{r})}{\partial r^\beta} - \sum_{\alpha, \mu} \mathcal{D}_\alpha^\mu \mathcal{L}_\alpha^\mu(\mathbf{r}) - \mathbf{B} \cdot \mathbf{m}(\mathbf{r}) - K (m^z(\mathbf{r}))^2 \right], \quad (2)$$

where

$$\mathcal{A}_{\alpha\beta} = \frac{1}{N} \sum_{i,j} J_{ij} (R_j^\alpha - R_i^\alpha)(R_j^\beta - R_i^\beta) \quad (3)$$

is the exchange stiffness tensor, and

$$\mathcal{D}_\alpha^\mu = \frac{1}{N} \sum_{i,j} D_{ij}^\mu (R_j^\alpha - R_i^\alpha) \quad (4)$$

is the DMI spiralization, and

$$\mathcal{L}_\alpha^\mu(\mathbf{r}) = \sum_{\nu, \eta} \varepsilon_{\mu\nu\eta} m^\nu(\mathbf{r}) \frac{\partial m^\eta(\mathbf{r})}{\partial r^\alpha} \quad (5)$$

are the Lifshitz invariants. Here α, β, γ label the Cartesian components of the position vector of each atom \mathbf{R} and of the continuum position \mathbf{r} for the magnetization vector field, and $\mu, \nu, \eta = x, y, z$ indicate the three components of the magnetization direction, with $\varepsilon_{\mu\nu\eta}$ the Levi-Civita symbol. V_0 is the volume per magnetic site and the sums run over all the N magnetic atoms for which the interactions are defined.

Complex magnetic states are explored through atomistic spin dynamic simulations using the Landau-Lifshitz-equation (LLG) as implemented in the Spirit code are performed using the Hamiltonian from Eq. 1. We employed boundary conditions to model the extended two-dimensional system on a lattice with 99×99 unit cells, each containing 3 spins.

Data availability The data that support the findings of this study is available from the corresponding author upon reasonable request.

Code availability The codes employed for the simulations described within this work are open-source and can be obtained from the respective websites and/or repositories. Quantum Espresso can be found at ⁷³, and the Jülich-developed codes JuKKR and Spirit can be found at ⁷⁴ and ⁷⁵, respectively.

Acknowledgements This work was supported by the China Scholarship Council program (H.Z.) and Outstanding Research Project of Shen Yuan Honors College, BUAA (230121102, H.Z.), the Priority Programmes SPP 2244 “2D Materials Physics of van der Waals heterobilayer” (project LO 1659/7-1, S.L.), SPP 2137 “Skyrmionics” (Projects LO 1659/8-1, S.L.) of the Deutsche Forschungsgemeinschaft (DFG), National Key Research and Development Program of China (2022YFB4400200, W.Z.), National Natural Science Foundation of China (92164206, W.Z.; 52121001, W.Z.), the New Cornerstone Science Foundation through the XPLOER PRIZE (W.Z.), CoSeC and the Computational Science Centre for Research Communities (CCP9, M.d.S.D.). Simulations were performed with computing resources granted by RWTH Aachen University under project p0020362 and JARA on the supercomputer JURECA ⁷⁶ at Forschungszentrum Jülich.

Author contributions S.L. initiated, designed and supervised the project. H.Z. performed the simulations with support and supervision from M.d.S.D and S.L. H.Z., M.d.S.D., Y.Z., W.Z. and S.L. discussed the results. H.Z., M.d.S.D and S.L. wrote the manuscript to which all co-authors contributed.

Competing interests The authors declare no competing interests.

References

1. Mekata, M. Kagome: the story of the basketweave lattice. *Phys. Today* **56**, 12–13 (2003). URL <https://doi.org/10.1063/1.1564329>. https://pubs.aip.org/physicstoday/article-pdf/56/2/12/11152056/12_1_online.pdf.
2. Fenner, L. A., Dee, A. A. & Wills, A. S. Non-collinearity and spin frustration in the itinerant kagome ferromagnet Fe_3Sn_2 . *J. Phys.: Condes. Matter* **21**, 452202 (2009). URL <https://dx.doi.org/10.1088/0953-8984/21/45/452202>.
3. Yin, J.-X. *et al.* Giant and anisotropic many-body spin–orbit tunability in a strongly correlated kagome magnet. *Nature* **562**, 91–95 (2018). URL <https://doi.org/10.1038/s41586-018-0502-7>.
4. Yin, J.-X. *et al.* Negative flat band magnetism in a spin-orbit-coupled correlated kagome magnet. *Nat. Phys.* **15**, 443–448 (2019). URL <https://doi.org/10.1038/s41567-019-0426-7>.
5. Sachdev, S. Kagomé- and triangular-lattice Heisenberg antiferromagnets: Ordering from quantum fluctuations and quantum-disordered ground states with unconfined bosonic spinons. *Phys. Rev. B* **45**, 12377–12396 (1992). URL <https://link.aps.org/doi/10.1103/PhysRevB.45.12377>.
6. Balents, L. Spin liquids in frustrated magnets. *Nature* **464**, 199–208 (2010). URL <https://doi.org/10.1038/nature08917>.

7. Mazin, I. I. *et al.* Theoretical prediction of a strongly correlated Dirac metal. *Nat. Commun.* **5**, 4261 (2014). URL <https://doi.org/10.1038/ncomms5261>.
8. Kang, M. *et al.* Dirac fermions and flat bands in the ideal kagome metal FeSn. *Nat. Mater.* **19**, 163–169 (2020). URL <https://doi.org/10.1038/s41563-019-0531-0>.
9. Tasaki, H. From Nagaoka’s ferromagnetism to flat-band ferromagnetism and beyond: An introduction to ferromagnetism in the Hubbard model. *Prog. Theor. Phys.* **99**, 489–548 (1998). URL <https://doi.org/10.1143/PTP.99.489>. <https://academic.oup.com/ptp/article-pdf/99/4/489/5209512/99-4-489.pdf>.
10. Mielke, A. Exact ground states for the Hubbard model on the Kagome lattice. *J. Phys. A: Math. Gen.* **25**, 4335 (1992). URL <https://dx.doi.org/10.1088/0305-4470/25/16/011>.
11. Pollmann, F., Fulde, P. & Shtengel, K. Kinetic ferromagnetism on a kagome lattice. *Phys. Rev. Lett.* **100**, 136404 (2008). URL <https://link.aps.org/doi/10.1103/PhysRevLett.100.136404>.
12. Kiesel, M. L., Platt, C. & Thomale, R. Unconventional fermi surface instabilities in the kagome hubbard model. *Phys. Rev. Lett.* **110**, 126405 (2013). URL <https://link.aps.org/doi/10.1103/PhysRevLett.110.126405>.
13. Ortiz, B. R. *et al.* CsV₃Sb₅: A \mathbb{Z}_2 topological kagome metal with a superconducting ground state. *Phys. Rev. Lett.* **125**, 247002 (2020). URL <https://link.aps.org/doi/10.1103/PhysRevLett.125.247002>.

14. Bolens, A. & Nagaosa, N. Topological states on the breathing kagome lattice. *Phys. Rev. B* **99**, 165141 (2019). URL <https://link.aps.org/doi/10.1103/PhysRevB.99.165141>.
15. Tang, E., Mei, J.-W. & Wen, X.-G. High-temperature fractional quantum hall states. *Phys. Rev. Lett.* **106**, 236802 (2011). URL <https://link.aps.org/doi/10.1103/PhysRevLett.106.236802>.
16. Kida, T. *et al.* The giant anomalous Hall effect in the ferromagnet Fe₃Sn₂—a frustrated kagome metal. *J. Phys.: Condes. Matter* **23**, 112205 (2011). URL <https://dx.doi.org/10.1088/0953-8984/23/11/112205>.
17. Liu, E. *et al.* Giant anomalous Hall effect in a ferromagnetic kagome-lattice semimetal. *Nat. Phys.* **14**, 1125–1131 (2018). URL <https://doi.org/10.1038/s41567-018-0234-5>.
18. Wang, Q. *et al.* Large intrinsic anomalous Hall effect in half-metallic ferromagnet Co₃Sn₂S₂ with magnetic weyl fermions. *Nat. Commun.* **9**, 3681 (2018). URL <https://doi.org/10.1038/s41467-018-06088-2>.
19. Nakatsuji, S., Kiyohara, N. & Higo, T. Large anomalous Hall effect in a non-collinear antiferromagnet at room temperature. *Nature* **527**, 212–215 (2015). URL <https://doi.org/10.1038/nature15723>.
20. Zhang, H., Feng, H., Xu, X., Hao, W. & Du, Y. Recent progress on 2D kagome magnets: Binary T_mSn_n (T = Fe, C, Mn). *Adv. Quantum Technol.* **4**, 2100073 (2021). URL <https://>

- onlinelibrary.wiley.com/doi/abs/10.1002/qute.202100073. <https://onlinelibrary.wiley.com/doi/pdf/10.1002/qute.202100073>.
21. Kang, M. *et al.* Topological flat bands in frustrated kagome lattice CoSn. *Nat. Commun.* **11**, 4004 (2020). URL <https://doi.org/10.1038/s41467-020-17465-1>.
 22. Yin, J.-X. *et al.* Fermion–boson many-body interplay in a frustrated kagome paramagnet. *Nat. Commun.* **11**, 4003 (2020). URL <https://doi.org/10.1038/s41467-020-17464-2>.
 23. Sales, B. C. *et al.* Electronic, magnetic, and thermodynamic properties of the kagome layer compound FeSn. *Phys. Rev. Mater.* **3**, 114203 (2019). URL <https://link.aps.org/doi/10.1103/PhysRevMaterials.3.114203>.
 24. Khadka, D. *et al.* Anomalous Hall and Nernst effects in epitaxial films of topological kagome magnet Fe₃Sn₂. *Phys. Rev. Mater.* **4**, 084203 (2020). URL <https://link.aps.org/doi/10.1103/PhysRevMaterials.4.084203>.
 25. Ye, L. *et al.* Massive Dirac fermions in a ferromagnetic kagome metal. *Nature* **555**, 638–642 (2018). URL <https://doi.org/10.1038/nature25987>.
 26. Rout, P. K., Madduri, P. V. P., Manna, S. K. & Nayak, A. K. Field-induced topological hall effect in the noncoplanar triangular antiferromagnetic geometry of Mn₃Sn. *Phys. Rev. B* **99**, 094430 (2019). URL <https://link.aps.org/doi/10.1103/PhysRevB.99.094430>.

27. Jiao, L. *et al.* Signatures for half-metallicity and nontrivial surface states in the kagome lattice Weyl semimetal $\text{Co}_3\text{Sn}_2\text{S}_2$. *Phys. Rev. B* **99**, 245158 (2019). URL <https://link.aps.org/doi/10.1103/PhysRevB.99.245158>.
28. Huang, L. *et al.* Discovery and construction of surface kagome electronic states induced by p - d electronic hybridization in $\text{Co}_3\text{Sn}_2\text{S}_2$. *Nat. Commun.* **14**, 5230 (2023). URL <https://doi.org/10.1038/s41467-023-40942-2>.
29. Ortiz, B. R. *et al.* Superconductivity in the \mathbb{Z}_2 kagome metal KV_3Sb_5 . *Phys. Rev. Mater.* **5**, 034801 (2021). URL <https://link.aps.org/doi/10.1103/PhysRevMaterials.5.034801>.
30. Yin, Q. *et al.* Superconductivity and normal-state properties of kagome metal RbV_3Sb_5 single crystals. *Chin. Phys. Lett.* **38**, 037403 (2021). URL <https://dx.doi.org/10.1088/0256-307X/38/3/037403>.
31. Ortiz, B. R. *et al.* New kagome prototype materials: discovery of KV_3Sb_5 , RbV_3Sb_5 , and CsV_3Sb_5 . *Phys. Rev. Mater.* **3**, 094407 (2019). URL <https://link.aps.org/doi/10.1103/PhysRevMaterials.3.094407>.
32. Jiang, K. *et al.* Kagome superconductors AV_3Sb_5 ($A = \text{K}, \text{Rb}, \text{Cs}$). *Natl. Sci. Rev.* **10**, nwac199 (2022). URL <https://doi.org/10.1093/nsr/nwac199>. <https://academic.oup.com/nsr/article-pdf/10/2/nwac199/49561488/nwac199.pdf>.

33. Lin, Z. *et al.* Flatbands and emergent ferromagnetic ordering in Fe_3Sn_2 kagome lattices. *Phys. Rev. Lett.* **121**, 096401 (2018). URL <https://link.aps.org/doi/10.1103/PhysRevLett.121.096401>.
34. Kim, S.-W., Oh, H., Moon, E.-G. & Kim, Y. Monolayer kagome metals AV_3Sb_5 . *Nat. Commun.* **14**, 591 (2023). URL <https://doi.org/10.1038/s41467-023-36341-2>.
35. Dean, C. R. *et al.* Boron nitride substrates for high-quality graphene electronics. *Nat. Nanotechnol.* **5**, 722–726 (2010). URL <https://doi.org/10.1038/nnano.2010.172>.
36. Katoch, J. *et al.* Giant spin-splitting and gap renormalization driven by trions in single-layer $\text{WS}_2/\text{h-BN}$ heterostructures. *Nat. Phys.* **14**, 355–359 (2018). URL <https://doi.org/10.1038/s41567-017-0033-4>.
37. Guimarães, M. H. D. *et al.* Controlling spin relaxation in hexagonal BN-encapsulated graphene with a transverse electric field. *Phys. Rev. Lett.* **113**, 086602 (2014). URL <https://link.aps.org/doi/10.1103/PhysRevLett.113.086602>.
38. Zihlmann, S. *et al.* Large spin relaxation anisotropy and valley-zeeman spin-orbit coupling in $\text{WSe}_2/\text{graphene}/\text{h-BN}$ heterostructures. *Phys. Rev. B* **97**, 075434 (2018). URL <https://link.aps.org/doi/10.1103/PhysRevB.97.075434>.
39. Lin, X., Yang, W., Wang, K. L. & Zhao, W. Two-dimensional spintronics for low-power electronics. *Nat. Electron.* **2**, 274–283 (2019). URL <https://doi.org/10.1038/s41928-019-0273-7>.

40. Hallal, A. *et al.* Rashba-type Dzyaloshinskii–Moriya interaction, perpendicular magnetic anisotropy, and skyrmion states at 2D materials/Co interfaces. *Nano Lett.* **21**, 7138–7144 (2021). URL <https://doi.org/10.1021/acs.nanolett.1c01713>. PMID: 34432472, <https://doi.org/10.1021/acs.nanolett.1c01713>.
41. Xie, Q. *et al.* Rashba–Edelstein effect in the h-BN van der Waals interface for magnetization switching. *Adv. Mater.* **34**, 2109449 (2022). URL <https://onlinelibrary.wiley.com/doi/abs/10.1002/adma.202109449>. <https://onlinelibrary.wiley.com/doi/pdf/10.1002/adma.202109449>.
42. El-Kerdi, B. *et al.* Evidence of strong Dzyaloshinskii–Moriya interaction at the cobalt/hexagonal boron nitride interface. *Nano Lett.* **23**, 3202–3208 (2023). URL <https://doi.org/10.1021/acs.nanolett.2c04985>. PMID: 37053437, <https://doi.org/10.1021/acs.nanolett.2c04985>.
43. Fert, A., Cros, V. & Sampaio, J. Skyrmions on the track. *Nat. Nanotechnol.* **8**, 152–156 (2013). URL <https://doi.org/10.1038/nnano.2013.29>.
44. Li, S. *et al.* Experimental demonstration of skyrmionic magnetic tunnel junction at room temperature. *Sci. Bull.* **67**, 691–699 (2022). URL <https://www.sciencedirect.com/science/article/pii/S2095927322000160>.
45. Guo, Z. *et al.* Spintronics for energy-efficient computing: An overview and outlook. *Proc. IEEE* **109**, 1398–1417 (2021).

46. Lynch, R. W. & Drickamer, H. G. Effect of high pressure on the lattice parameters of diamond, graphite, and hexagonal boron nitride. *J. Chem. Phys.* **44**, 181–184 (2004). URL <https://doi.org/10.1063/1.1726442>. https://pubs.aip.org/aip/jcp/article-pdf/44/1/181/11155148/181_1_online.pdf.
47. Waseda, Y., Hirata, K. & Ohtani, M. High-temperature thermal expansion of platinum, tantalum, molybdenum, and tungsten measured by x-ray diffraction. *High Temp.-High Press.* **7**, 221–226 (1975). URL http://inis.iaea.org/search/search.aspx?orig_q=RN:07233088.
48. Maeland, A. & Flanagan, T. B. Lattice spacings of gold–palladium alloys. *Can. J. Phys.* **42**, 2364–2366 (1964). URL <https://doi.org/10.1139/p64-213>. <https://doi.org/10.1139/p64-213>.
49. Liu, L. & Bassett, W. A. Compression of Ag and phase transformation of NaCl. *J. Appl. Phys.* **44**, 1475–1479 (2003). URL <https://doi.org/10.1063/1.1662396>. https://pubs.aip.org/aip/jap/article-pdf/44/4/1475/7949833/1475_1_online.pdf.
50. Laskowski, R., Blaha, P. & Schwarz, K. Bonding of hexagonal BN to transition metal surfaces: An *ab initio* density-functional theory study. *Phys. Rev. B* **78**, 045409 (2008). URL <https://link.aps.org/doi/10.1103/PhysRevB.78.045409>.
51. Bokdam, M., Brocks, G., Katsnelson, M. I. & Kelly, P. J. Schottky barriers at hexagonal boron nitride/metal interfaces: A first-principles study. *Phys. Rev. B* **90**, 085415 (2014). URL

<https://link.aps.org/doi/10.1103/PhysRevB.90.085415>.

52. Müller, F., Stöwe, K. & Sachdev, H. Symmetry versus commensurability: Epitaxial growth of hexagonal boron nitride on Pt(111) from B-trichloroborazine (Cl₃BNH₃). *Chem. Mater.* **17**, 3464–3467 (2005). URL <https://doi.org/10.1021/cm048629e>. <https://doi.org/10.1021/cm048629e>.
53. Grad, G. B., Blaha, P., Schwarz, K., Auwärter, W. & Greber, T. Density functional theory investigation of the geometric and spintronic structure of *h*-BN/Ni(111) in view of photoemission and STM experiments. *Phys. Rev. B* **68**, 085404 (2003). URL <https://link.aps.org/doi/10.1103/PhysRevB.68.085404>.
54. Zhou, Y., Zu, X. & Gao, F. Substrate-induced magnetism in BN layer: A first-principles study. *Solid State Commun.* **151**, 883–886 (2011). URL <https://www.sciencedirect.com/science/article/pii/S003810981100175X>.
55. Friedel, J. & Sayers, C.M. On the role of d-d electron correlations in the cohesion and ferromagnetism of transition metals. *J. Phys. France* **38**, 697–705 (1977). URL <https://doi.org/10.1051/jphys:01977003806069700>.
56. Deplante, J. & Blandin, A. Effets de taille et interactions chimiques dus aux impuretés de transition dans les métaux normaux. *J. Phys. Chem. Solids* **26**, 381–389 (1965). URL <https://www.sciencedirect.com/science/article/pii/0022369765901678>.

57. Nonas, B., Wildberger, K., Zeller, R. & Dederichs, P. H. Energetics of 3d impurities on the (001) surface of iron. *Phys. Rev. Lett.* **80**, 4574–4577 (1998). URL <https://link.aps.org/doi/10.1103/PhysRevLett.80.4574>.
58. Nonas, B., Wildberger, K., Zeller, R., Dederichs, P. H. & Gyorffy, B. L. Magnetic properties of 4d impurities on the (001) surfaces of nickel and iron. *Phys. Rev. B* **57**, 84–87 (1998). URL <https://link.aps.org/doi/10.1103/PhysRevB.57.84>.
59. Leonov, A. O. & Kézsmárki, I. Asymmetric isolated skyrmions in polar magnets with easy-plane anisotropy. *Phys. Rev. B* **96**, 014423 (2017). URL <https://link.aps.org/doi/10.1103/PhysRevB.96.014423>.
60. Everschor-Sitte, K., Masell, J., Reeve, R. M. & Kläui, M. Perspective: Magnetic skyrmions—Overview of recent progress in an active research field. *J. Appl. Phys.* **124**, 240901 (2018). URL <https://doi.org/10.1063/1.5048972>.
https://pubs.aip.org/aip/jap/article-pdf/doi/10.1063/1.5048972/15217991/240901_1_online.pdf.
61. Moon, K.-W., Yoon, J., Kim, C. & Hwang, C. Existence of in-plane magnetic skyrmion and its motion under current flow. *Phys. Rev. Appl.* **12**, 064054 (2019). URL <https://link.aps.org/doi/10.1103/PhysRevApplied.12.064054>.
62. Lin, Y.-H. *et al.* Fabrication and imaging monatomic Ni Kagome lattice on superconducting Pb(111). *Nano Lett.* **22**, 8475–8481 (2022). URL <https://doi.org/10.1021/>

- [acs.nanolett.2c02831](https://doi.org/10.1021/acs.nanolett.2c02831). PMID: 36282025, <https://doi.org/10.1021/acs.nanolett.2c02831>.
63. Park, S. *et al.* Kagome van-der-Waals Pd₃P₂S₈ with flat band. *Sci. Rep.* **10**, 20998 (2020). URL <https://doi.org/10.1038/s41598-020-77825-1>.
64. Sun, Z. *et al.* Observation of topological flat bands in the kagome semiconductor Nb₃Cl₈. *Nano Lett.* **22**, 4596–4602 (2022). URL <https://doi.org/10.1021/acs.nanolett.2c00778>. PMID: 35536689, <https://doi.org/10.1021/acs.nanolett.2c00778>.
65. Giannozzi, P. *et al.* QUANTUM ESPRESSO: a modular and open-source software project for quantum simulations of materials. *J. Phys.: Condes. Matter* **21**, 395502 (2009). URL <https://dx.doi.org/10.1088/0953-8984/21/39/395502>.
66. Grimme, S., Antony, J., Ehrlich, S. & Krieg, H. A consistent and accurate *ab initio* parametrization of density functional dispersion correction (DFT-D) for the 94 elements H-Pu. *J. Chem. Phys.* **132**, 154104 (2010). URL <https://doi.org/10.1063/1.3382344>. https://pubs.aip.org/aip/jcp/article-pdf/doi/10.1063/1.3382344/15684000/154104_1_online.pdf.
67. Dal Corso, A. Pseudopotentials periodic table: From H to Pu. *Comp. Mater. Sci.* **95**, 337–350 (2014). URL <https://www.sciencedirect.com/science/article/pii/S0927025614005187>.

68. Perdew, J. P., Burke, K. & Ernzerhof, M. Generalized gradient approximation made simple. *Phys. Rev. Lett.* **77**, 3865–3868 (1996). URL <https://link.aps.org/doi/10.1103/PhysRevLett.77.3865>.
69. Papanikolaou, N., Zeller, R. & Dederichs, P. H. Conceptual improvements of the KKR method. *J. Phys.: Condes. Matter* **14**, 2799 (2002). URL <https://dx.doi.org/10.1088/0953-8984/14/11/304>.
70. Bauer, D. S. G. *Development of a relativistic full-potential first-principles multiple scattering Green function method applied to complex magnetic textures of nano structures at surfaces*. Ph.D. thesis, Aachen, Techn. Hochsch., Diss., 2013 (2014).
71. Liechtenstein, A., Katsnelson, M., Antropov, V. & Gubanov, V. Local spin density functional approach to the theory of exchange interactions in ferromagnetic metals and alloys. *J. Magn. Magn. Mater.* **67**, 65–74 (1987). URL <https://www.sciencedirect.com/science/article/pii/0304885387907219>.
72. Ebert, H. & Mankovsky, S. Anisotropic exchange coupling in diluted magnetic semiconductors: *Ab initio* spin-density functional theory. *Phys. Rev. B* **79**, 045209 (2009). URL <https://link.aps.org/doi/10.1103/PhysRevB.79.045209>.
73. Website: <https://www.quantum-espresso.org>.
74. Repository: <https://github.com/JuDFTteam/JuKKR>.
75. Website: <https://spirit-code.github.io>.

76. Jülich Supercomputing Centre. JURECA: Data centric and booster modules implementing the modular supercomputing architecture at Jülich supercomputing centre. *Journal of large-scale research facilities* **7**, A182 (2021). URL <http://dx.doi.org/10.17815/jlsrf-7-182>.